Interoperability and Misalignment Tolerance of Electric Vehicle Wireless Charging System Based on Multiple Self-Decoupled Transmitting Coils and Vector Synthesis Strategy

Yiming Zhang, *Senior Member, IEEE*, Zhongjin Huang, Zhiwei Shen, Ronghuan Xie, *Graduate Student Member, IEEE*, Xiaoying Chen, and Xingkui Mao, *Member, IEEE*

***Abstract*—In wireless power transfer (WPT) systems for electric vehicles (EVs), interoperability and misalignment tolerance for different receiving charging terminals meet great demands. In this article, a hybrid topology with a vector synthesis strategy and highly integrated magnetic couplers are proposed to achieve misalignment tolerance and interoperability for unipolar (Q), bipolar (DD), and quadrupolar (QUA) coils over the *X* and *Y* misalignments. By adjusting the phase angles of the four half-bridge inverters under different misalignments, the output voltage fluctuation can be limited. The mathematical model of the proposed hybrid topology is established and the vector synthesis strategy is introduced. The magnetic couplers and the design principle are presented. A 2-kW prototype is built to verify the proposed system. The experimental results demonstrate that the output voltage fluctuation under misalignments is less than 3.1% for the *Rx* Q coil, 3.3% for the *Rx* DD coil, and 4.3% for the *Rx* QUA coil, and the peak efficiency is 89.3%.**

***Index Terms*—Highly integrated magnetic couplers, hybrid topology, interoperability, misalignment tolerance, vector synthesis strategy, wireless power transfer (WPT).**

I. Introduction

In order to adapt to the development of green concepts in the new era, the design research of electric vehicles (EVs) are more in-depth, and the technological innovation and replacement are getting faster and faster. The development of EVs has also been accompanied by technological innovation [1], [2], [3]. The onboard charger [4], [5] has become increasingly mature today, and its reliable construction and high-efficiency power transmission make it occupy a large market of EV charging. Compared with conductive charging, wireless power transfer (WPT) has the advantages of convenience and safety which means the EVs can be charged once parked to the designated area without touching the charging device. Therefore, the structures and control mode of WPT have been continuously optimized in recent years [6], [7] and it can be applied in portable consumer electronics [8], autonomous underwater vehicle [9], industrial robot [10], and so on.

As a method of WPT, inductive power transfer (IPT) based on magnetic coupling has been widely used. An IPT system [11] usually includes power converters, magnetic couplers, and resonant networks. The magnetic couplers are made up of the transmitting (*Tx*) and receiving (*Rx*) coils. For static charging, when the EV stops, the charging location of the EV is uniquely determined. But the Rx usually does not align well with the *Tx*. This will cause the output fluctuation and the decreased efficiency. Therefore, misalignment tolerance is a critical problem for the WPT systems. Meanwhile, due to the fact that the *Tx* and the *Rx* are separate, they can be fabricated by different manufacturers. Thus, the *Tx* and the *Rx* can be different in terms of coil type, compensation network, power level, etc. There exist different *Rx* coil designs in existing standards such as J2954 from Society of Automotive Engineers. This can introduce the problem of interoperability. The simultaneous implementation of interoperability and misalignment tolerance requires the optimization of topology, coil structure, and appropriate strategies. The schematic of the WPT system and the interoperability are shown in Fig. 1.

In terms of misalignment, the door-door and front-rear misalignments can frequently happen in an EV wireless charging system. The tolerance for the door-door misalignment is more critical since drivers can adjust the EV forward or backward easily but it is not convenience for door-door adjustment. To achieve misalignment tolerance on both directions, the topology, magnetic couplers, and the control strategy should be specially designed. There have been various articles on above three aspects.

The basic compensation networks include series (S), parallel (P), inductor-capacitor-capacitor (*LCC*), and inductor-capacitor-inductor (*LCL*). These above four networks can be combined

Received 8 July 2024; revised 9 October 2024 and 16 December 2024; accepted 29 December 2024. Date of publication 6 January 2025; date of current version 26 February 2025. This work was supported in part by the National Natural Science Foundation of China under Grant 52107183 and Grant 52407197, and in part by the Natural Science Foundation of Fujian Province under Grant 2022J06011. Recommended for publication by Associate Editor K.-B. Park. *(Corresponding authors: Xiaoying Chen; Xingkui Mao.)*

The authors are with the School of Electrical Engineering and Automation, Fuzhou University, Fuzhou 350108, China (e-mail: zym@fzu.edu.cn; 220120026@fzu.edu.cn; 240110013@fzu.edu.cn; 230127018@fzu.edu.cn; fzucxy@fzu.edu.cn; mxk782@fzu.edu.cn).

Color versions of one or more figures in this article are available at https://doi.org/10.1109/TPEL.2025.3526136.

Digital Object Identifier 10.1109/TPEL.2025.3526136

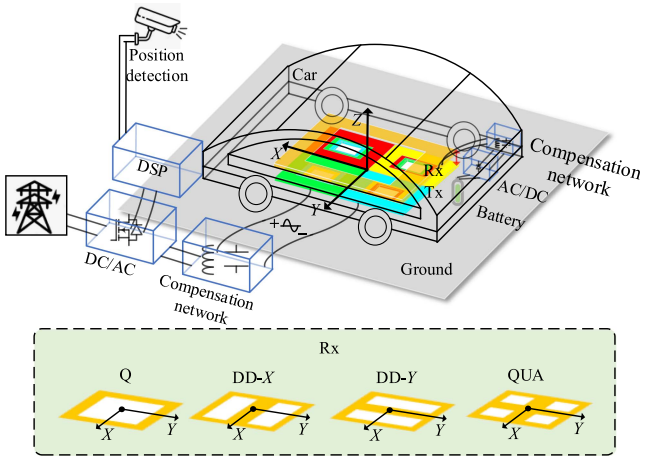

Fig. 1. Schematic of the WPT system and the interoperability.

as a new compensation at the *Tx* or *Rx* sides. In [12], two input-parallel-output-series S-S topologies and a variable inductor were used to smooth the output with the output power fluctuation. A dc-controlled variable inductor was adopted in [13] to tolerate coupling coefficient change. A double-sided *CLLLC* topology was adopted in [14] with the output fluctuation within 5%. The capacitance tuning was employed for both CC output and misalignment tolerance in [15]. Using the reconfigurable and detuned topology can ensure 20% power fluctuation in an ultra-wide coupling coefficient range (from 0.07 to 0.33) [16]. The magnetic coupler is another significant part in the WPT system. Unipolar coils (Q), bipolar coils (DD), and quadrupolar coils (QUA), solenoid coils are the four basic types of the couplers. The series solenoid and DD pads was proposed to improve the misalignment tolerance in [17]. Four special L-shaped coils were connected in series as the *Rx* coil in [18] to achieve a stable output under misalignment. A dual coupled antiparallel coil was proposed in [19] for misalignment tolerance. The phase shift control can be used as the control strategy to achieve misalignment tolerance. In [20], the phase shift was used to tolerate the load-independent output current. By controlling the current phase shift of the *Tx*, a constant output power under misalignment could be realized [21]. All these studies only consider the misalignment tolerance for a specific type of *Rx*. The design for misalignment tolerance and interoperability should be investigated.

The evaluation of interoperability performance was studied in [22]. The compatibility analysis of the quadruple coil structure with the Q, the DD, and the DDQ structures were explored [23]. In [24], the proposed asymmetrical quadrupolar coil could be interoperable with conventional coils under misalignments. But the fluctuations of the output were large. An interoperable transmitter composed of two adjacent unipolar coils and a three-switch dual-output inverter was proposed in [25]. However, only the issue of the interoperability between Q and DD could be solved. The weak interoperability between rectangular coil and double-D pad could be improved through adjusting the pad's relative position [26]. The decoupled mutually spliced double-D (DD) receiving coils which can achieve certain interoperability and misalignment tolerance is proposed in [27]. A new decoupling method and a quadrupole receiving coil with series-connected diode rectifiers for interoperability was proposed in [28].

TABLE I
CROSS MUTUAL INDUCTANCES OF MAGNETIC COUPLERS

Parameter	Symbol	Value
Coupling coefficient of Tx_1 and Tx_2	k_{12}	0.012
Coupling coefficient of Tx_1 and Tx_3	k_{13}	−0.012
Coupling coefficient of Tx_1 and Tx_4	k_{14}	0.007
Coupling coefficient of Tx_2 and Tx_3	k_{23}	0.009
Coupling coefficient of Tx_2 and Tx_4	k_{24}	−0.005
Coupling coefficient of Tx_3 and Tx_4	k_{34}	0.007

Some recent studies have focused on both interoperability and misalignment. But it is difficult to maintain high misalignment tolerance while satisfying interoperability. This article proposes a four-*LCC*-parallel topology, the highly integrated *Tx* coils, and the vector synthesis strategy to achieve compatibility with different *Rx* coils and a low output fluctuation [29].

The rest of this article is organized as follows. Section II presents the mathematical model of the proposed topology and the principle of the vector synthesis strategy. The design process and the decoupling principle of the magnetic couplers are clarified in Section III. The experimental results and the comparisons with other studies are presented in Section IV. Finally, Section V concludes this article.

II. PROPOSED MAGNETIC COUPLERS

The structures of magnetic couplers are presented in Fig. 2(a), and the decomposition diagram of the transmitting coils is depicted in Fig. 2(b). The transmitting distance is 75 mm. The magnetic coupler consists of the *Tx* part and the *Rx* part. The *Tx* part is three layers and it is made up of the transmitting coils, ferrite and compensation inductances. The transmitting coils are placed under the ferrite and the compensation inductances are placed on the ferrite. The *Rx* can be Q, DD-*X*, DD-*Y* (DD placed along *X*- or *Y*-axis) or QUA. Mutual decoupling between coils is vital to the performance of WPT. In this article, four coils of the *Tx* are decoupled with each other. Every *Tx* coil includes a main coil and another two nested coils which are nested in the adjacent coils clockwise. The coupling relationship between Tx_1, Tx_2 in Fig. 2(b) are taken as an example to illustrate the method of decoupling. Since the direction of the excitation current of each coil is counterclockwise, the mutual inductance of the two coils nested into each other is positive ($[L_{A1}, L_{S2}]$, $[L_{D1}, L_{A2}]$), while that of two adjacent coils is negative ($[L_{S1}, L_{S2}]$, $[L_{S1}, L_{A2}]$, $[L_{S1}, L_{D2}]$, $[L_{A1}, L_{A2}]$, $[L_{A1}, L_{D2}]$, $[L_{D1}, L_{D2}]$). Sum of these mutual inductances tend to be zero after size design. Above analysis apply equally to any two other Tx coils. the decoupling between the four nonoverlapping Q coils can be realized. The cross-coupling coefficients of the *Tx* coils which given in Table I are so low that they can decouple with each other.

To reduce the volume of the system, the compensation inductors are integrated into the *Tx* side. The two adjacent DD which

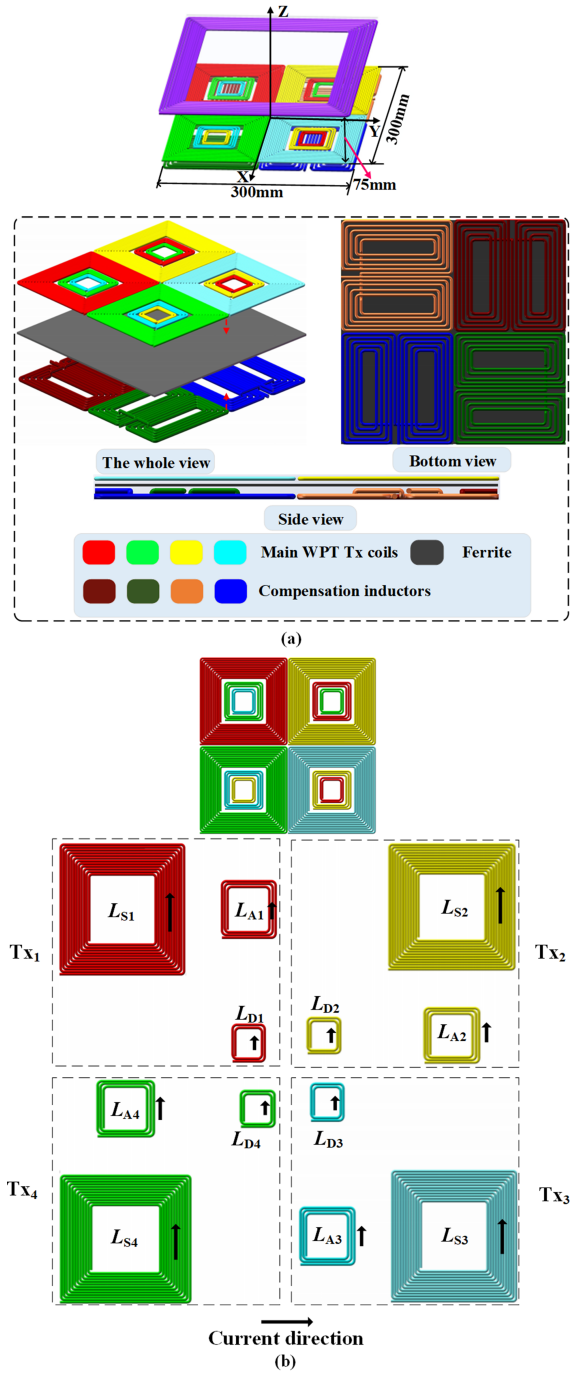

Fig. 2. (a) Structure of the magnetic couplers. (b) Decomposition diagram of the transmitting coils.

are placed orthogonal to each other are decoupled from each other. In the meantime, due to the magnetic shielding effect of ferrite, the compensation inductors are decoupled from the *Tx* coils and the *Rx* coils.

III. Proposed Topology and Mathematical Model

A. Proposed Topology

The *LCC-S* topology is selected to tolerate weak couplings, as shown in Fig. 3(a). The corresponding magnetic couplers are shown in Fig. 3(b). In Fig. 3(b), *Tx* is the transmitting side on the ground, which consists of compensation inductors, ferrite and transmitting coils. *Rx* is the receiving side, which consists of the receiving coils and ferrite. The receiving coil can be a Q coil, a DD coil placed along the *X*- or *Y*-directions (DD-*X* or DD-*Y* coils hereinafter), or a QUA coil. S_1-S_8 are eight power MOSFETs of the inverter. The inputs of the four half-bridge inverters are connected in parallel. D_1-D_4 are the rectifier diodes. Four *LCC* compensation networks are connected with four parallel half-bridge inverters. $L_{P1} \sim L_{P4}$ are the compensation inductances, placed underneath the ferrite plate. They are four DD coils and perpendicularly arranged so that they are decoupled from each other. The mutual inductances between compensation inductances and between the compensation inductances and *Rx* are not considered. Because the mathematical model is complex with much types of cross coupling, and each branch cannot be controlled independently. $L_1 \sim L_4$ are the *Tx* coils, placed above the ferrite plate. They are four unipolar coils and adjacently placed on the same plane. A nested coil technique is employed to achieve decoupling of the four *Tx* coils, which will be explained in Section III. L_R is the *Rx* coil. $C_1 \sim C_4$, $C_{P1} \sim C_{P4}$, and C_R are the compensating capacitances. R_L is the load resistance. V_{INV} and V_{REC} represent the dc voltages of the inverter and rectifier, respectively. $\boldsymbol{U}_{I1} \sim \boldsymbol{U}_{I4}$ denote the ac input voltage. $\boldsymbol{U}_{\text{OUT}}$ denotes the ac output voltage. $\boldsymbol{I}_{P1} \sim \boldsymbol{I}_{P4}$, $\boldsymbol{I}_1 \sim \boldsymbol{I}_4$, and $\boldsymbol{I}_R$ denote the rms values of the corresponding currents. $M_1 \sim M_4$ are the mutual inductances and they are scalar quantity. Mutual inductance is positive or negative which is relative to the direction of magnetic field

$$M_m = k_m M e_m \quad (m = 1,\ 2,\ 3\,\text{or}\,4,\ k_m = +1\,\text{or}\,-1) \tag{1}$$

where *Me* is modulus. When $k = +1$, it means that the direction of the magnetic field is the same as that of the reference branch, and vice versa.

Assume the four *Tx* branches are identical, namely

$$L_{Pm} = L_P,\ L_m = L_T,\ C_{Pm} = C_P, C_m = C_T. \tag{2}$$

B. Mathematical Modeling

The angular frequency of the system is ω. The resonant conditions of the WPT system can be expressed as

$$\omega L_P - \frac{1}{\omega C_P} = \omega L_R - \frac{1}{\omega C_R} = \omega L_T - \frac{1}{\omega C_T} - \frac{1}{\omega C_P} = 0. \tag{3}$$

Using fundamental harmonic approximation, the relationship between the ac and dc quantities can be deduced as

$$U_{\text{Im}} = \frac{\sqrt{2}}{\pi} V_{\text{INV}}, \quad U_{\text{OUT}} = \frac{2\sqrt{2}}{\pi} V_{\text{REC}}. \tag{4}$$

By phase shift of the four half-bridge inverters, the four ac input voltage vectors can be expressed as

$$\boldsymbol{U}_{\text{Im}} = U_{\text{Im}} \angle \theta_m \tag{5}$$

where θ_m is the phase of the ac input voltage. The vectors are in bold in this article.

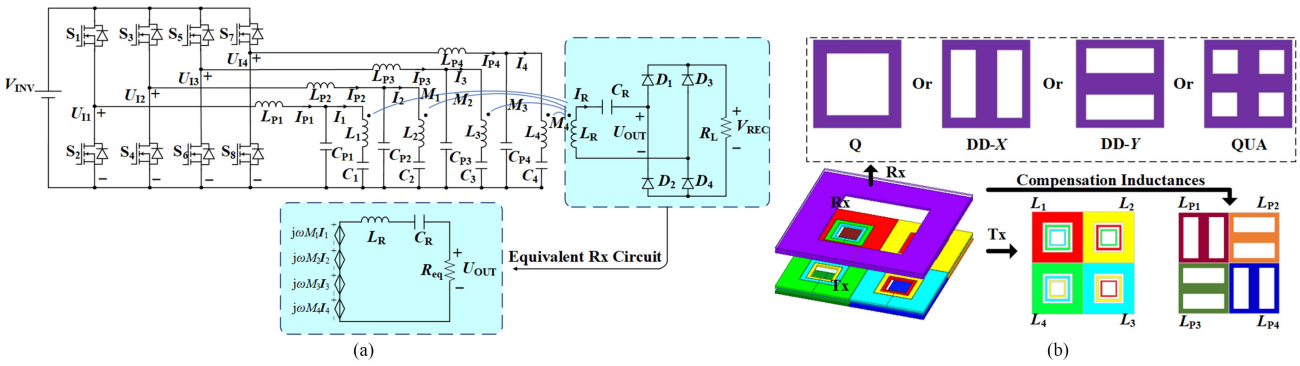

Fig. 3. Proposed interoperable and misalignment tolerant WPT system. (a) Topology and the equivalent *Rx* circuit. (b) Magnetic couplers.

By analyzing the circuit of Fig. 3(a), the Kirchhoff's law of voltage (KVL) equations can be expressed as

$$\begin{cases} \boldsymbol{U}_{\mathrm{Im}} = j\omega L_{Pm}\boldsymbol{I}_{Pm} + \frac{1}{j\omega C_{Pm}}\left(\boldsymbol{I}_{Pm} - \boldsymbol{I}_m\right) \\ \left(\mathrm{j}\omega L_m + \frac{1}{j\omega C_m}\right)\boldsymbol{I}_m + \frac{1}{j\omega C_{Pm}}\left(\boldsymbol{I}_m - \boldsymbol{I}_{Pm}\right) \\ \qquad -j\omega M_m \boldsymbol{I}_R = 0 \\ \sum_{m=1}^{4} j\omega M_m \boldsymbol{I}_m = \left(j\omega L_m + \frac{1}{j\omega C_R}\right)\boldsymbol{I}_R + \boldsymbol{U}_{\mathrm{OUT}} \end{cases} . \quad (6)$$

By solving (6), the compensating inductance currents and the *Tx* coil currents can be deduced as

$$I_{Pm} = \omega^2 C_{Pm} M_m I_R \quad (7)$$

$$I_m = \frac{\sqrt{2}}{\pi}\omega C_{Pm} V_{\mathrm{INV}}. \quad (8)$$

It can be seen that I_{Pm} is determined by M_m and I_{R}, while I_m is solely determined by $\mathrm{V_{INV}}$.

The ac and dc output voltage, the output power and the efficiency can be obtained as

$$V_{\mathrm{REC}} = \frac{\pi}{2\sqrt{2}}U_{\mathrm{OUT}} = \frac{\omega^2 C_P V_{\mathrm{INV}}\left|\sum_{m=1}^{4} M_m \angle\theta_m\right|}{2} \quad (9)$$

$$P_{\mathrm{OUT}} = \frac{\omega^4 C_P^2 V_{\mathrm{INV}}^2\left|\sum_{m=1}^{4} M_m \angle\theta_m\right|^2}{4R_L} \quad (10)$$

$$\eta = \frac{P_{\mathrm{OUT}}}{P_{\mathrm{OUT}} + P_{\mathrm{LOSS}-LP} + P_{\mathrm{LOSS}-L} + P_{\mathrm{LOSS}-LR}} = \frac{P_{\mathrm{OUT}}}{P_{\mathrm{OUT}} + \sum_{j=1}^{4} I_{Pj}^2 R_{Pj} + \sum_{j=1}^{4} I_j^2 R_j + I_R^2 R_R} \quad (11)$$

where R_{Pm}, R_m, and R_R are the parasitic resistances of the compensation inductances $L_{\mathrm{P}m}$, the *Tx* coil L_m, and the *Rx* coil L_R, respectively. $P_{\mathrm{LOSS}\text{-}LP}$, $P_{\mathrm{LOSS}\text{-}L}$, and $P_{\mathrm{LOSS}\text{-}LR}$ are the losses of the compensating inductances, the *Tx* coils, and the *Rx* coil, respectively. They are defined as

$$P_{\mathrm{LOSS}-LP} = \sum_{j=1}^{4} I_{Pm}^2 R_{Pm}, P_{\mathrm{LOSS}-L} = \sum_{j=1}^{4} I_m^2 R_m, P_{\mathrm{LOSS}-LR} = I_R^2 R_R. \quad (12)$$

The volatility δ the output voltage is defined as follows:

$$\delta = \frac{U_{\text{out - max}} - U_{\text{out - min}}}{U_{\text{out - max}} + U_{\text{out - min}}} \times 100\% \quad (13)$$

where $U_{\text{out-max}}$ and $U_{\text{out-min}}$ are the maximum and minimum values of U_{out}, respectively.

The mathematical model is built on the basis of ignoring cross coupling. In order for each branch to work independently, the *Tx* coils need to decouple each other. In the meanwhile, the compensation inductors need to decouple each other, and decouple with *Tx* and *Rx*. The magnetic coupler design for above purposes.

C. Topology When Coupling Exists Between L_{Pi} and Between L_{Pi} and Rx

Coupling only exists between L_i and *Rx* in the proposed topology in Fig. 3(a). The reasons for choosing this topology are explained in this part. The topology of wireless charging system is generally designed to have a load-independent constant voltage (CV) or a load-independent constant current (CC) output characteristic. The two-channel topology when coupling exists between L_{Pi} and between L_{Pi} and *Rx* are depicted in Fig. 4(a) and (b), respectively. By writing KVL equations for the two topologies in Fig. 4, the output current can be deduced as

$$\boldsymbol{I}_R = \frac{\omega^2 C_{P1} M_1 \boldsymbol{U}_{I1} + \omega^2 C_{P2} M_2 \boldsymbol{U}_{I2}}{R_{\mathrm{eq}} + 2j\omega^5 C_{P1} C_{P2} M_{P12} M_1 M_2} \quad (14)$$

$$\boldsymbol{I}_R = \frac{\omega^2 C_{P1} M_1 \boldsymbol{U}_{I1} + \omega^2 C_{P2} M_2 \boldsymbol{U}_{I2}}{R_{\mathrm{eq}} - 2j\omega^3 C_{P1} M_{P1} M_1 - 2j\omega^3 C_{P2} M_{P2} M_2} \quad (15)$$

where (14) and (15) are the output ac current of Fig. 4(a) and (b), respectively.

The R_{eq} exists in (14) and (15), which means the output characteristic are complex and they are neither CC nor CV. The introduction of multiple variables will cause the complexity of the system, making it difficult to control the system to achieve the desired output characteristic. And the efficiency also may be decreased.

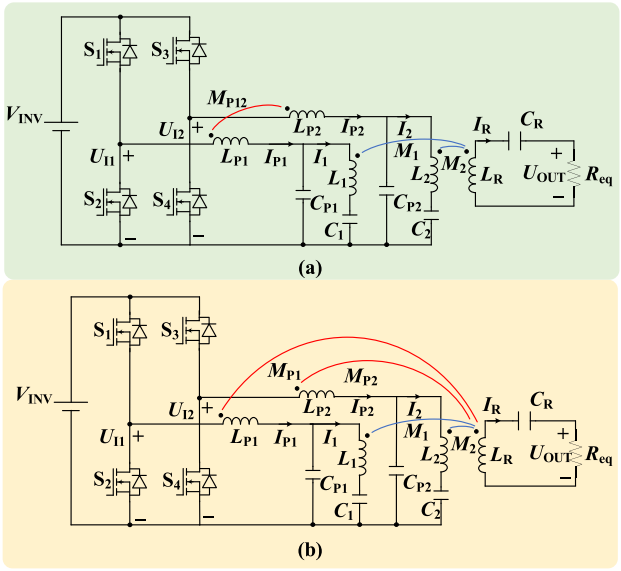

Fig. 4. (a) Topology with coupling between L_{Pi}. (b) Topology with coupling between L_{Pi} and *Rx*.

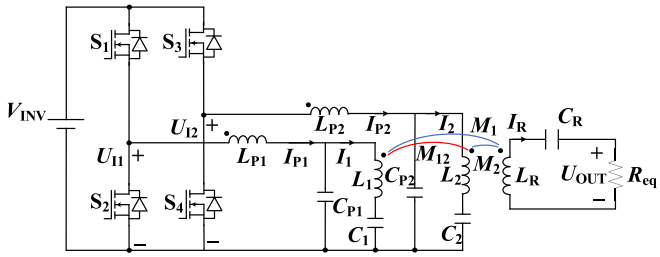

Fig. 5. Topology with coupling exists between L_i.

D. Loop Current Analysis When Coupling Exists Between L_i

To analyze the loop current of the system, a two-channel topology with coupling exists between L_i are depicted in Fig. 5. M_{12} is the cross mutual inductance. The first energy channel applies an induced voltage to the second energy channel through M_{12}, and the second energy channel does the same. The induced voltage can be express as

$$\boldsymbol{U}_{12} = j\omega M_{12}\boldsymbol{I}_1 \tag{16}$$

$$\boldsymbol{U}_{21} = j\omega M_{12}\boldsymbol{I}_2 \tag{17}$$

where $\boldsymbol{U}_{12}$ is the induced voltage of the first channel on the second channel, and $\boldsymbol{U}_{21}$ is the opposite. These two voltages will create the loop current in the corresponding loop. The loop current will affect $\boldsymbol{I}_{P1}$ and $\boldsymbol{I}_{P2}$, and they can be expressed by (18) and (19) shown at the bottom of this page. It can be found that the loop current will increase the reactive power, and some

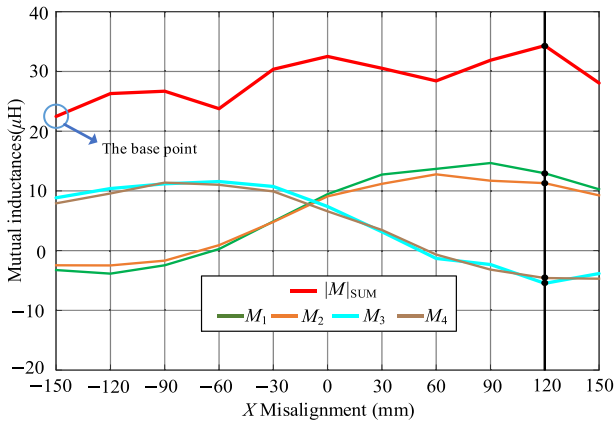

Fig. 6. M_1-M_4 and sum of absolute values of M_1-M_4 under *X* misalignment for the *Rx* Q.

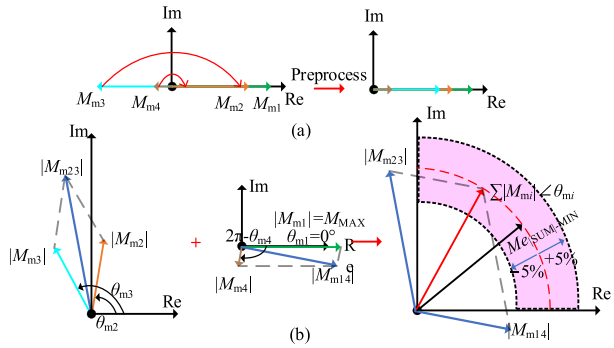

Fig. 7. (a) Preprocess. (b) Vector synthesis strategy.

energy transmission may even be offset compared with (7) and (8). Due to the above reasons, the output current state of each inverter will be affected and the efficiency of the system may be reduced. Therefore, the content of Section II is important, and the design of magnetic coupler can minimize the influence of mutual inductance under the condition of allowing appropriate cross mutual inductance

IV. Vector Synthesis Strategy

It can be seen that the output characteristic of this system is load-independent constant voltage from (9). From Fig. 3(a), the regulation of the output voltage is related to the superposition of the induced voltage of the four branches on the receiving coil. In (9), only $\sum \boldsymbol{M}_m\angle\theta_m$ is a variable. So here $\sum \boldsymbol{M}_m\angle\theta_m$ is defined as the equivalent transmitting mutual inductance as the research object, while the sum of induced voltages is not used as the analysis object.

This part introduces the fundamental principle of vector synthesis in detail. The sum of each absolute value and the maximum

$$\boldsymbol{I}_{P1} = \frac{\omega^4 C_{P1}^2 M_1^2}{R_{\text{eq}}}\boldsymbol{U}_{I1} + \left(j\omega^3 C_{P1}C_{P2}M_{12} + \frac{\omega^4 C_{P1}C_{P2}M_1M_2}{R_{\text{eq}}}\right)\boldsymbol{U}_{I2} \tag{18}$$

$$\boldsymbol{I}_{P2} = \left(j\omega^3 C_{P1}C_{P2}M_{12} + \frac{\omega^4 C_{P1}C_{P2}M_1M_2}{R_{\text{eq}}}\right)\boldsymbol{U}_{I1} + \frac{\omega^4 C_{P2}^2 M_2^2}{R_{\text{eq}}}\boldsymbol{U}_{I2}. \tag{19}$$

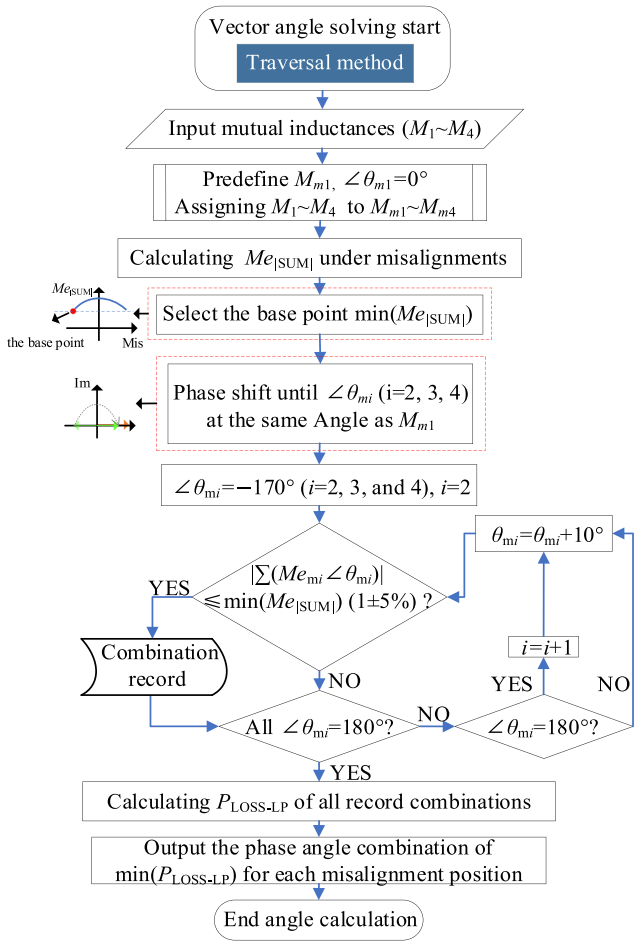

Fig. 8. Flow chart of vector synthesis strategy.

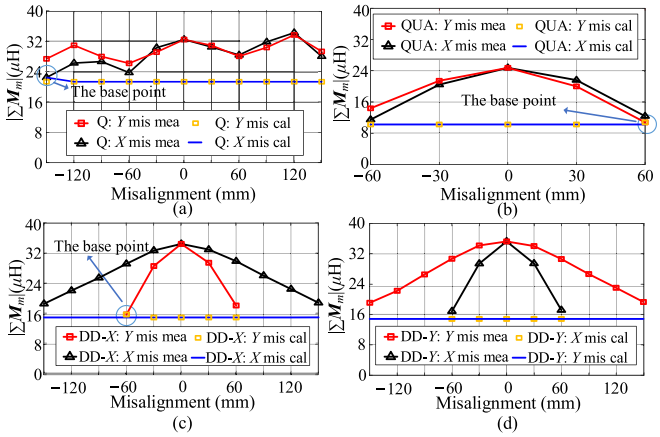

Fig. 9. $\sum|M_j|$ under different misalignments. (a) Q. (b) QUA. (c) DD-*X*. (d) DD-*Y*.

value of the four mutual inductances are defined, respectively, as

$$Me_{|\mathrm{SUM}|} = \sum_{m=1}^{4} Me_m \tag{20}$$

$$Me_{\mathrm{MAX}} = \max\{Me_1,\ Me_2,\ Me_3,\ Me_4\} \tag{21}$$

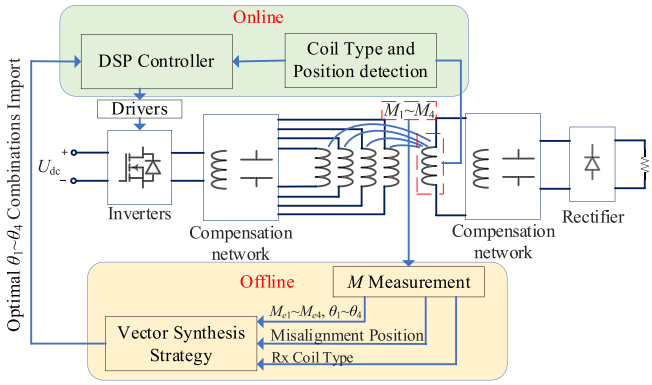

Fig. 10. Control diagram of the proposed WPT system.

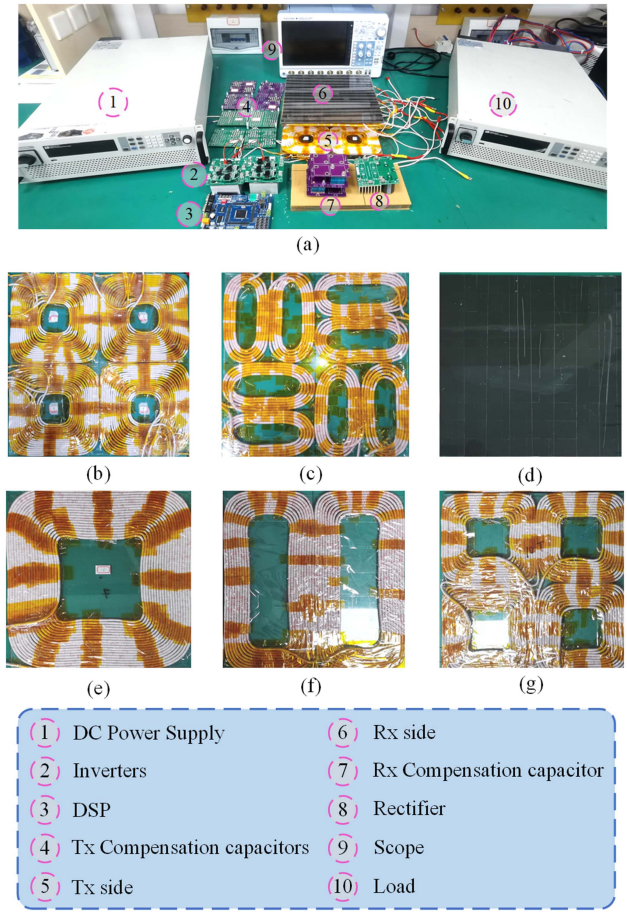

Fig. 11. Experimental protoype. (a) Hardware prototype. (b) *Tx* coils. (c) Compensation inductances. (d) Ferrite. (e) *Rx* Q. (f) *Rx* DD. (g) *Rx* QUA.

where M_e is the absolute value of M_m without phase.

A. Vector Synthesis Strategy for One Misalignment Position

The first step of vector synthesis is to solve the optimal phase combination of the three receiving coils at each offset position. The Q coil is utilized as the example when *X* misalignment is 120 mm in Section IV-A. M_1-M_4 and sum of absolute values $|M_e|_{\mathrm{SUM}}$ of M_1-M_4 under *X* misalignment for the *Rx* Q ($|M_e|_{\mathrm{SUM}} = \sum M_{ei}$) are depicted in Fig. 6. When *X*

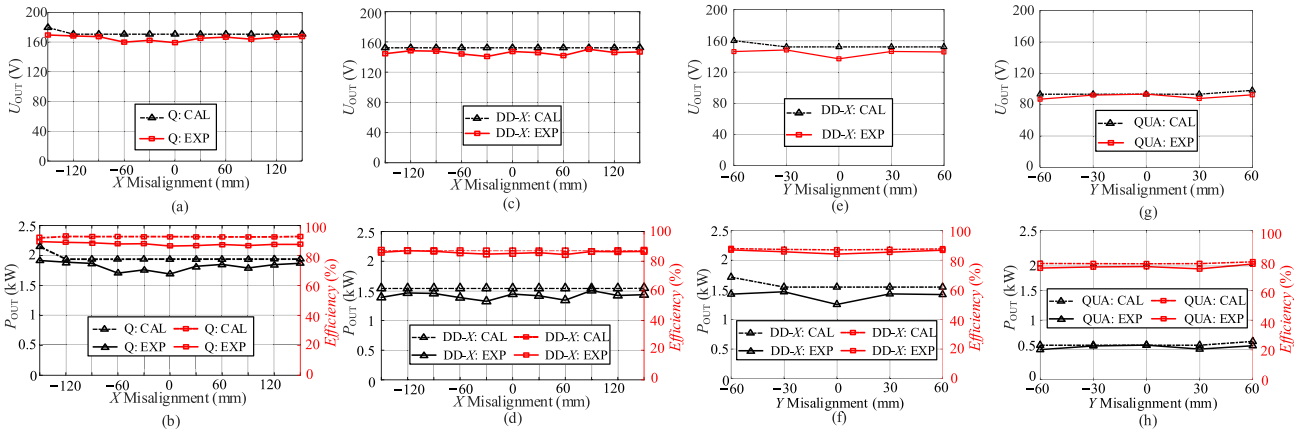

Fig. 12. Calculated and experimental output voltage, output power and DC–DC efficiency of the *Rx* Q, DD-*X* and quad under misalignments. (a) and (b) *Rx* Q under *X* misalignments. (c) and (d) *Rx* DD-*X* under *X* misalignments. (e) and (f) *Rx* DD-*X* under *Y* misalignments. (g) and (f) *Rx* quad under *Y* misalignments.

TABLE II
PHASE ANGLES COMBINATION OF THE *RX* Q UNDER *X* MISALIGNMENTS

X misalignments (mm)	θ_1	θ_2	θ_3	θ_4
−150	180°	180°	0°	0°
−120	−160°	−110°	0°	0°
−90	−160°	−110°	0°	0°
−60	−170°	−160°	0°	0°
−30	−40°	30°	0°	10°
0	0°	−80°	40°	0°
30	0°	−50°	90°	20°
60	0°	20°	10°	10°
90	0°	−50°	−80°	−90°
120	0°	−70°	−150°	−100°

TABLE III
PARAMETERS OF EXPERIMENTAL PROTOTYPE

V_{INV}	200 V	f	85 kHz	R_L	15 Ω
L_{P1}	11.02 μH	L_1	41.40 μH	$L_{Rx\text{-}Q}$	194.4 μH
L_{P2}	11.68 μH	L_2	41.63 μH	$L_{Rx\text{-}DD}$	115.7 μH
L_{P3}	10.70 μH	L_3	42.26 μH	$L_{Rx\text{-}Quad}$	110.3 μH
L_{P4}	11.24 μH	L_4	43.73 μH	$C_{Rx\text{-}Q}$	18 nF
C_{P1}	311.9 nF	C_1	115 nF	$C_{Rx\text{-}DD}$	30.3 nF
C_{P2}	296.3 nF	C_2	117.9 nF	$C_{Rx\text{-}Quad}$	31.77 nF

TABLE IV
COMPARISON BETWEEN OPTIMAL AND WORSE PHASE COMBINATION WHEN THE *RX* ALIGNS WELL WITH THE *TX*

Q	$[\theta_1, \theta_2, \theta_3, \theta_4]$	$\sum {I_{Pm}}^2$	U_{OUT}	Efficiency
Optimal	[0°, −80°, 40°, 0°]	**329**	159.2 V	**86.3%**
Worse	[0°, −80°, 30°, −60°]	351	154.3 V	84.2%
DD-*Y*	$[\theta_1, \theta_2, \theta_3, \theta_4]$	$\sum {I_{Pm}}^2$	U_{OUT}	Efficiency
Optimal	[150°, 20°, 0°, 50°]	**228**	144.4 V	**84.77%**
Worse	[150°, 20°, 0°, −130°]	273	136.8 V	82.56%
QUA	$[\theta_1, \theta_2, \theta_3, \theta_4]$	$\sum {I_{Pm}}^2$	U_{OUT}	Efficiency
Optimal	[−20°, −30°, −120°, 0°]	**62**	93.5 V	**76.0%**
Worse	[−20°, −70°, 180°, 0°]	67	97.8 V	73.5%

misalignment is −150 mm, the $|M|_{SUM}$ is minimum, and it is selected as the base point. When *X* misalignment is 120 mm, M_1, $M_2 > 0$, M_3, $M_4 < 0$, and $|M_1| > |M_2| > |M_3| > |M_4|$. M_1-M_4 are assigned to M_{m1}-M_{m4} in descending order. M_{m1} is selected as the reference vector, and its phase is set as 0°. The voltage excitation phase of the switches of the branches with the opposite coupling relationship to M_{m1} needed to be flipped like Fig. 7(a). After preprocess, the four output of the four transmitting branches are superimposed forward.

In order to obtain the phase angles of M_{m2}-M_{m4} and synthesize the desired vector (value of the base point) within a certain error, the phases of the M_{m2}-M_{m4} are traversed from 0 to 180° at the intervals of 10° like Fig. 7(b). In this case, 5% is selected as the tolerant error and it can be other values according to the requirements. The synthesized vector which is indicated by a red line for each misalignment position must fall within the pink region. For the offset position as the base point, only the preprocess is needed. For the other position, there are many phase combinations that can satisfy the above condition, but only one optimal phase combination is selected. The principles for selecting the optimal combination of phase angles are described in the next part.

B. Principle of Vector Synthesis Strategy

Obtaining the optimal combination of phase angles at each offset distance is the focus of this strategy. By restricting the synthesized vector within the pink ring, a variety of phase angle combinations can be obtained. But only one combination is needed. The principle of minimum loss is utilized as the criterion for determining the optimal phase angle combination.

From (7) and (8), it can be concluded that I_{Pm} depends on M_m, indicating that I_{Pm} changes with positions. Thus, $P_{LOSS\text{-}LP}$ varies with positions. I_m is independent of M_m, indicating that I_m remains constant at any positions. Thus, $P_{LOSS\text{-}L}$ is constant. To maintain a stable output, I_R should be constant. Thus, $P_{LOSS\text{-}LR}$ is constant. In the efficiency expression, only $P_{LOSS\text{-}LP}$ changes with positions. When $P_{LOSS\text{-}LP}$ is minimized, the efficiency would be the highest. Therefore, the criterion for

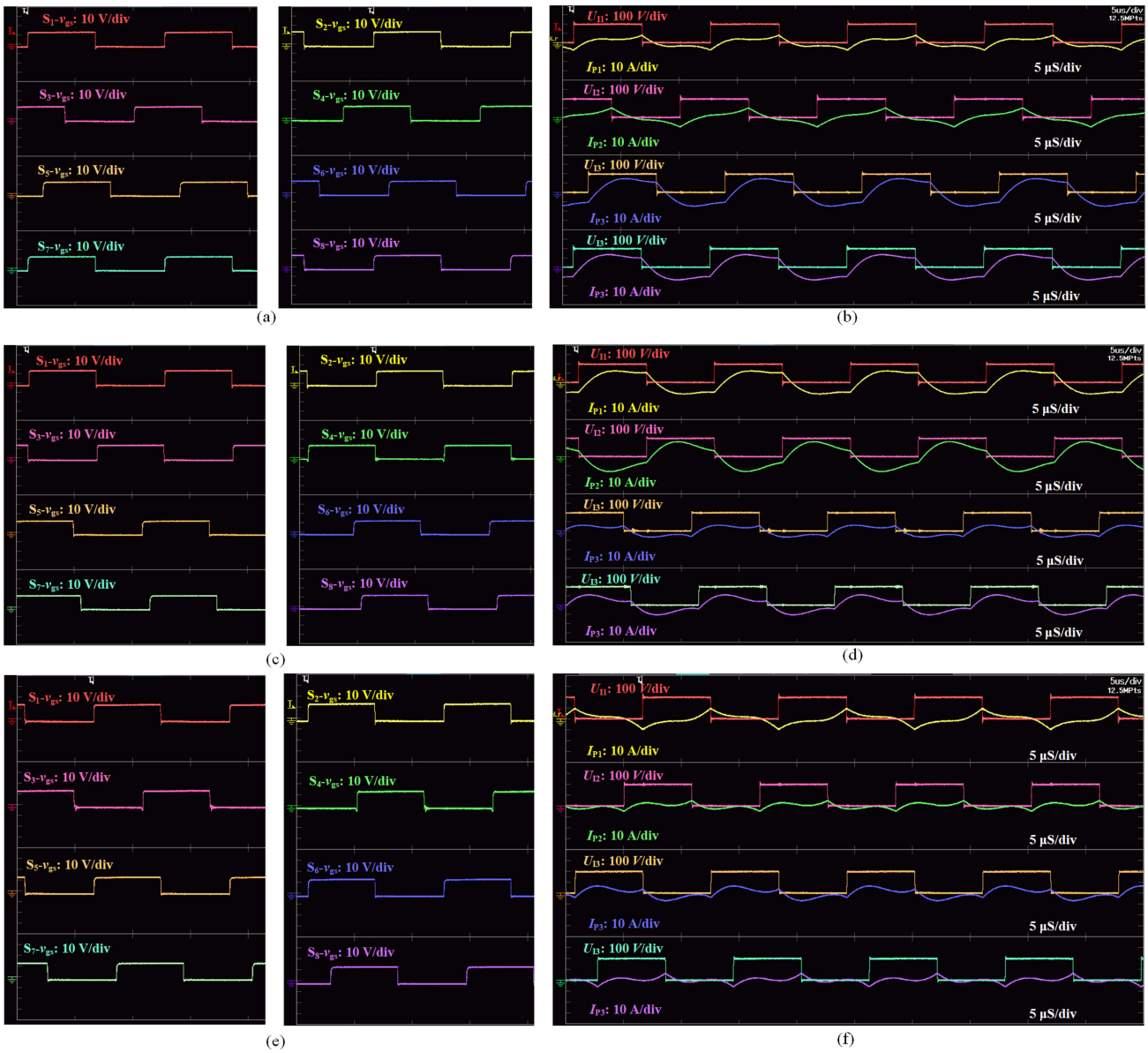

Fig. 13. Driving waveforms v_{gs} of S_1-S_8 and experimental waveforms of U_{I1}-U_{I4} and I_{P1}-I_{P4} when *Tx* well align with *Rx*. (a) and (b) *Rx* Q. (c) and (d) *Rx* DD-*X*. (e) and (f) *Rx* QUA.

selecting the phase shift angles is to minimize $P_{\text{LOSS-}LP}$. Thus, the objective function can be expressed as

$$f(I_{Pm}(\theta_m, M_m)) = \min_{(\text{Mis}X,\text{Mis}Y)} \left(\sum_{j=1}^{4} I_{Pm}^2 R_{Pm} \right)$$
$$\text{s.t} \begin{cases} -170^\circ < \theta_m < 180^\circ \ m = 1,\ 2,\ 3 \text{ or } 4 \\ \sum_{m=1}^{4} |M_m| \angle\theta_m \le (1 \pm 5\%)\, M_{|\text{SUM}|-\text{MIN}} \end{cases}. \quad (22)$$

Through the aforementioned introduction, the vector synthesis flow chart as shown in Fig. 8 can be obtained. The optimal phase angle combinations for each offset position of the three Rx coils will be calculated by the flow chart.

C. Synthesized Mutual Inductances of Three Types of Coils

The $|\sum \boldsymbol{M}_m|$ under misalignments of three types of the *Rx* coils are depicted in Fig. 9. The measured values mean the sum of absolute values of mutual inductance of four branches actually measured without phase shift processing. The calculated values mean the modulus of the equivalent transmitting mutual inductances. It can be seen that the curve of equivalent transmitting mutual inductance becomes smooth after vector synthesis calculation. In Fig. 9, the misalignments range is $-60 \sim 60$ mm for QUA, DD-*X*: *Y* misalignment and DD-*Y*: *X* misalignment, while others are all -150 mm-150 mm. Based on the strategy in Section II, the $Me_{|\text{SUM}|-\text{MIN}}$ which can also be called as the base point are circled in a blue box in Fig. 9. It should be noted that one type of coil has only one base point. The

TABLE V
COMPARISON WITH OTHER METHODS

Comparison	Tx Coil	Misalignment Range (mm) (Misalignment Percentage)	Interoperable types	Output Fluctuation
Xie et al. [25]	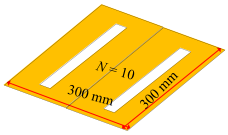	Q: *X*- and *Y*- misalignment: −150 – 150 mm (50%) DD-*X*: *Y*- misalignment: −90 – 90 mm (30%)	2	Q: 15.7% DD-*X*: 12.7%
Zhang et al. [28]	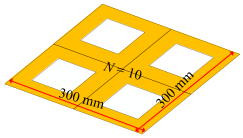	Q: *X*- and *Y*- misalignment: −150 – 150 mm (50%) DD-*X*: *X*- and *Y*- misalignment: −150 – 150 mm (50%)	2	Q: 6.1% DD-*X*: 42.5%
Zhang et al. [24]	Same to [28]	Q: *X*- and *Y*- misalignment: −30 – 210 mm DD: *X*- misalignment: −210 – 60 mm *Y*- misalignment: −60 – 210 mm QUA: *X*- and *Y*- misalignment: −210 – 60 mm	3	Large
This article	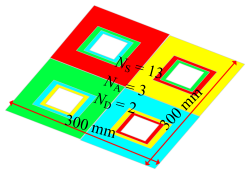	**Q: *X*- and *Y*- misalignment: ±150 mm (50%)** **DD-*X*: *X*- misalignment: ±60 mm (20%)** ***Y*- misalignment: ±150 mm (50%)** **QUA: *X*- and *Y*- misalignment: ±60 mm (20%)**	**3**	**Q: 3.1%** **DD-*X*: 3.3%** **QUA: 4.3%**

DD-*X* and DD-*Y* have a common base point. For the *Rx* Q coil, the base point is when the *X* misalignment is −150 mm. For the Rx DD-*X* and DD-*Y*, the base point is when the *Y* misalignment of DD-*X* is −60 mm. Based on the vector synthesis strategy, the resultant equivalent mutual inductance curve will be one with a limited range of volatility as the blue line and square symbols in Fig. 9. The line will close to a straight line. According to the base point and the measured mutual inductances, the phase angles $\theta_1 \sim \theta_4$ can be traversed by the vector synthesis strategy. Due to the length of the paper, only the phase angles of the *Rx* Q under *X* misalignments are displayed in Table II.

D Hardware Implementation of Vector Synthesis Strategy

The control diagram of the proposed WPT system has been depicted in Fig. 10. The control of this article is divided into two parts, including the offline part of the design stage and the online control part. In the off-line part, the parameters of the three types of receiving coils are measured under misalignment at first, and then the optimal phase combinations calculated by vector synthesis strategy are introduced to digital signal processor (DSP). In the online part, the After the position detection, the DSP will output the corresponding signal to the driver to control the opening and closing of the switches of the inverters.

V. EXPERIMENTAL VALIDATION

To verify the availability of the proposed system, a 2-kW prototype is built. The experimental prototype is shown in Fig. 11. The parameters of the experimental prototype are given in Table III. In Table III, $N_{Tx\text{-}LS}$, $N_{Tx\text{-}LA}$, and $N_{Tx\text{-}LD}$ are the turns of the *Tx* coils and their nested coils which are shown in Fig. 2(b). $N_{Rx\text{-}Q}$, $N_{Rx\text{-}DD}$, and $N_{Rx\text{-QUA}}$ are the turns of the corresponding *Rx* coils.

A. Output Characteristic

The calculated and experimental output voltage of the *Rx* Q, DD-*X*, and QUA under *X* or *Y* misalignments are depicted in Fig. 12. The experiments were all done with both *X* and *Y* misalignments for all types of the *Rx* coils. But due to the near consistency of the output of the same *Rx* in the process of *X* and *Y* misalignment, this article only shows the calculated and experimental output voltage, output power and dc–dc efficiency of the *Rx* Q under *X* misalignments, the *Rx DD-X* under *X* and *Y* misalignments and the *Rx* QUA under *Y* misalignments, respectively.

It can be concluded from Fig. 12 that the experimental results are slightly less than the calculated results and generally agree well with the calculated results. The output voltage curves are smoother after vector synthesis as the $|\sum \boldsymbol{M}_m|$ in Fig. 9. The δ of output voltage is 3.1% for the *Rx* Q, 3.3% for the *Rx* DD and 4.3% for the *Rx* QUA. The results of the δ of output voltage are all within the default range 5%. The peak output power is 1917 W for the *Rx* Q, 1506 W for the *Rx* DD and 582 W for the *Rx* QUA. The average dc–dc efficiency is 87.5% the *Rx* Q, 85.6% for the *Rx* DD and 75.76% for the *Rx* QUA. When the *Rx* is a QUA, the overall output power and the average efficiency are low. Because the structure of QUA will result in the low mutual inductances, and the energy transmission will be inadequate. There exist some discrepancies between calculated and experimental results like the asymmetry of the figure. The asymmetry of the figures can be caused by the asymmetry of the

hand-wound *Tx* coils and the actual experimental model has a slight error with the mathematical model.

B. Verification of the Optimal Combination

In order to verify whether the combinations of the phase angles obtained meets the principle of minimum $P_{\text{LOSS-}LP}$ when the Rx is under misalignments, another phase angles combination that meet the restriction conditions are compared with the optimal phase angel combination when the *Rx* aligns well with the *Tx* which is shown as Table IV. It can be concluded that the optimal combinations calculated by the vector synthesis strategy have a lower $\sum I_{Pm}^2$ and a higher efficiency. The accuracy of the strategy can be verified.

The driving waveforms v_{gs} of S1-S8 and the experimental waveforms of U_{I1}-U_{I4} and I_{P1}-I_{P4} when the *Tx* well align with the *Rx* for the three types of the *Rx* coils are depicted in Fig. 13. Fig. 13 shows the actual operation of the phase synthesis strategy. The phase of voltage is slightly ahead of the phase of current in these two randomly selected misalignment positions, which proves that the transmit-side impedance shows weak inductance. Zero voltage switching has been realized for the three types of *Rx* coils under different misalignments, which can actually decrease the loss of switches and stable output.

C. Comparison

In order to show the superiority of the proposed system, the performance of the proposed method has been compared with the other methods in Table V. For magnetic couplers structure, compared to [28], the transmitting coils can be integrated with the compensation inductors, reducing the system size. Compared to [25], there are more interoperable coil types. Compared to [24], the output fluctuation is smaller and misalignment tolerance is better with the same compatible coil type.

VI. Conclusion

This article has proposed a WPT system based on the topology combined four transmitting coils and a receiving coil. The transmitting side consisted of four parallel *LCC* compensation networks, and four *Tx* coils were decoupled with each other. The compensation inductances were also integrated into the *Tx* side to reduce system volume. A vector synthesis strategy was proposed to improve misalignment tolerance. By adjusting the phase angles of the four half-bridge inverters, the load-independent output voltage can be reduced to the voltage of the base point. The mathematical model of the topology was established and analyzed. The vector synthesis strategy was introduced by a schema and a flow chart in detail. Parameters of magnetic couplers were displayed and the phase angles combinations were calculated to achieve a better misalignment performance of the proposed system. A 2-kW experimental prototype was implemented to verify the effectiveness of the vector synthesis strategy and the IPT system.

References

[1] Z. Shen, R. Xie, C. Liu, X. Yu, X. Cheng, and Y. Zhang, "An electric vehicle wireless charging system with 400-V and 800-V battery tolerance and strong offset resistance," *IEEE Trans. Power Electron.*, 2025, to be published, doi: 10.1109/TPEL.2024.3516715.

[2] A. Ahmad, M. S. Alam, and R. Chabaan, "A comprehensive review of wireless charging technologies for electric vehicles," *IEEE Trans. Transport Electrific.*, vol. 4, no. 1, pp. 38–63, Nov. 2017.

[3] W. Pan, R. Liu, R. Xie, Y. Zhuang, X. Mao, and Y. Zhang, "A multi-output modular wireless power transfer system with constant-current characteristic," *IEEE Trans. Power Electron.*, 2024, to be published, doi: 10.1109/TPEL.2024.3512656.

[4] M. Yilmaz and P. T. Krein, "Review of battery charger topologies, charging power levels, and infrastructure for plug-in electric and hybrid vehicles," *IEEE Trans. Power Electron.*, vol. 28, no. 5, pp. 2151–2169, May 2013.

[5] Y. Wu et al., "An integrated charger of wireless power transfer, onboard charger, and auxiliary power module for electric vehicles," *IEEE Trans. Power Electron.*, 2025, to be published, doi: 10.1109/TPEL.2024.3518499.

[6] E. Rong, P. Sun, G. Yang, J. Xia, Z. Liu, and S. Li, "5-kW, 96.5% efficiency capacitive power transfer system with a five-plate coupler: Design and optimization," *IEEE Trans. Power Electron.*, vol. 40, no. 1, pp. 2542–2555, Jan. 2025.

[7] Y. Zhang, H. Zhou and Z. Shen, R. Xie, X. Chen, and X. Mao, "An interoperable dynamic wireless charging system with stable output based on a self-adaptive two-pole receiver," *IEEE Trans. Power Electron.*, vol. 39, no. 10, pp. 11943–11947, Oct. 2024.

[8] P. Zhao, X. Ji, H. Wang, and M. Fu, "H5-bridge-based bowl-shape wireless charger for multiple loads," *IEEE Trans. Ind Electron.*, vol. 70, no. 9, pp. 8853–8861, Sep. 2023.

[9] H. Tang et al., "A self-adaptive dual-channel LCC-S detuned topology for misalignment tolerance in AUV wireless power transfer systems," *IEEE Trans. Power Electron.*, vol. 40, no. 3, pp. 4630–4639, Mar. 2025, to be published, doi: 10.1109/TPEL.2024.3492194.

[10] J. Wu, X. Dai, R. Gao, and J. Jiang, "A coupling mechanism with multidegree freedom for bidirectional multistage WPT system," *IEEE Trans. Power Electron.*, vol. 36, no. 2, pp. 1376–1387, Feb. 2021.

[11] V. Vu et al., "Operation of inductive charging systems under misalignment conditions: A review for electric vehicles," *IEEE Trans Transport. Electrific.*, vol. 9, no. 1, pp. 1857–1887, Mar. 2023.

[12] Z. Li, H. Liu, Y. Huo, J. He, and Y. Tian, and J. Liu, "High-misalignment tolerance wireless charging system for constant power output using dual transmission channels with magnetic flux controlled inductors," *IEEE Trans. Power Electron.*, vol. 37, no. 11, pp. 13930–13945, Nov. 2022.

[13] Z. Zhang et al., "A dynamic wireless power transfer system using DC-controlled variable inductor for segment transmitter automatic switching," *IEEE Trans. Ind Electron.*, vol. 40, no. 1, pp. 23–27, Jan. 2025.

[14] B. Yang, Y. Chen, W. Ruan, H. Liu, Y. Ren, and R. Mai, "Current stress optimization for double-sided CLLLC topology-based IPT system with constant output current tolerating pad misalignments," *IEEE Trans. Power Electron.*, vol. 32, no. 6, pp. 4659–4369, Aug. 2016.

[15] C. Cai, J. Wang, M. Saaeedifard, P. Zhang, R. Chen, and J. Zhang, "Gyrator-gain variable WPT topology for MC-unconstrained CC output customizaion using simplified capacitance tuning," *IEEE Trans. Ind Electron.*, vol. 71, no. 4, pp. 3594–3605, Apr. 2024.

[16] P. Zhao, J. Liang, H. Wang, and M. Fu, "Detuned LCC/SS compensation for stable-output inductive power transfer system under ultrawide coupling variation," *IEEE Trans. Power Electron.*, vol. 38, no. 10, pp. 12342–12347, Jul. 2023.

[17] J. Mai, Y. Wang, Y. Yao, M. Sun, and D. Xu, "High-misalignment-tolerant IPT systems with solenoid and double D pads," *IEEE Trans. Ind Electron.*, vol. 69, no. 4, pp. 3527–3535, Apr. 2022.

[18] X. Zhang, X. Ma, Z. Yuan, F. Xu, Z. Chen, and F. Wang, "Misalignment-tolerant integration for S-LCC-compensated WPT systems: A complementary-coupling compact receiver," *IEEE Trans. Power Electron.*, vol. 38, no. 10, pp. 11907–11915, Oct. 2023.

[19] Y. Zhang, H. Zhou, R. Xie, X. Mao, X. Chen, and Z. Li, "A smooth-output dynamic wireless charging system for automated guided vehicles with dual-receiver magnetic coupler," *IEEE Trans. Power Electron.*, 2025, to be published, doi: 10.1109/TPEL.2024.3516042.

[20] M. Wu et al., "A compact coupler with integrated multiple decoupled coils for wireless power transfer system and its anti-misalignment control," *IEEE Trans. Power Electron.*, vol. 37, no. 10, pp. 12814–12827, Oct. 2022.

[21] X. Li, B. Sun, J. Xu, S. Pang, and H. Li, "Design and analysis of misalignment insensitive wireless power transfer system based on multitransmitter for constant power," *IEEE J. Emerg. Sel. Topics Power Electron.*, vol. 11, no. 4, pp. 4536–4548, Apr. 2023.
[22] G. Yang et al., "Improved interoperability evaluation method for wireless charging systems based on interface impedance," *IEEE Trans. Power Electron.*, vol. 36, no. 8, pp. 8588–8592, Aug. 2021.
[23] A. Ahmad, M. S. Alam, and A. A. S. Mohamed, "Design and interoperability analysis of quadruple pad structure for electric vehicle wireless charging application," *IEEE Trans Transport. Electrific.*, vol. 5, no. 4, pp. 934–945, Dec. 2019.
[24] Y. Zhang, C. Liu, M. Zhou, and X. Mao, "A novel asymmetrical quadrupolar coil for interoperability of unipolar, bipolar, and quadrupolar coils in electric vehicle wireless charging systems," *IEEE Trans. Ind Electron.*, vol. 71, no. 4, pp. 4300–4303, Apr. 2024.
[25] R. Xie, R. Liu, X. Chen, X. Mao, X. Li, and Y. Zhang, "An interoperable wireless power transmitter for unipolar and bipolar receiving coils based on three-switch dual-output inverter," *IEEE Trans. Power Electron.*, vol. 39, no. 2, pp. 1985–1989, Feb. 2024.
[26] G. Yang et al., "Interoperability improvement for rectangular pad and dd pad of wireless electric vehicle charging system based on adaptive position adjustment," *IEEE T IND APPL*, vol. 57, no. 3, pp. 2613–2624, May/Jun. 2021.
[27] W. Pan, C. Liu, H. Tang, Y. Zhuang, and Y. Zhang, "An interoperable electric vehicle wireless charging system based on mutually spliced double-D coil," *IEEE Trans. Power Electron.*, vol. 39, no. 3, pp. 3864–3872, Mar. 2024.
[28] Y. Zhang et al., "A quadrupole receiving coil with series-connected diode rectifiers for interoperability of nonpolarized and polarized transmitting coils," *IEEE Trans. Power Electron*, vol. 38, no. 7, pp. 8000–8004, Jul. 2023.
[29] Z. Huang, R. Xie, and W. Pan, "Integrated four-LCC-parallel circuit for wireless power transfer of electric vehicles with vector synthesis strategy," in *Proc. IEEE 19th Conf. Ind. Electron. Appl.*, 2024, pp. 1–6, doi: 10.1109/ICIEA61579.2024.10665269.

Yiming Zhang (Senior Member, IEEE) received the B.S. and Ph.D. degrees in electrical engineering from Tsinghua University, Beijing, China, in 2011 and 2016, respectively.

Afterward, he was a Postdoctoral Researcher with San Diego State University, San Diego, CA, USA and a Research Fellow with Nanyang Technological University, Singapore. He is currently a Full Professor with Fuzhou University. He has authored 1 book from Springer, authored or co-authored more than 100 technical papers in journals and conference proceedings. His research interests include wireless power transfer and resonant converters.

Dr. Zhang was the recipient of the Outstanding Doctoral Dissertations of Tsinghua University in 2016. He was recognized as an Outstanding Reviewer for IEEE TRANSACTIONS ON POWER ELECTRONICS in 2019 and 2022, and a Distinguished Reviewer for IEEE TRANSACTIONS ON INDUSTRIAL ELECTRONICS in 2020. He was the Publication Chair of the international conference ICWPT2022.

Zhongjin Huang was born in Fujian, China. He is currently working toward the master's degree in power electronics with the School of Electrical Engineering and Automation, Fuzhou University, Fuzhou, China.

His research direction includes wireless power transfer.

Zhiwei Shen was born in Nanping, China. He is currently working toward the Ph.D. degree in power electronics with the School of Electrical Engineering and Automation, Fuzhou University, Fuzhou, China.

His research direction includes wireless power transfer.

Ronghuan Xie (Graduate Student Member, IEEE) was born in Fujian, China. He is currently working toward the master's degree in power electronics with the School of Electrical Engineering and Automation, Fuzhou University, Fuzhou, China.

His research direction includes wireless power transfer.

Xiaoying Chen received the Ph.D. degree in electrical engineering from Central South University, Changsha, China, in 2023.

He is currently a Lecturer with the College of Electrical Engineering and Automation, Fuzhou University, Fuzhou, China.

Xingkui Mao (Member, IEEE) received the B.E. and Ph.D. degrees in electrical engineering from Fuzhou University, Fuzhou, China, in 2000 and 2006 respectively.

He is currently a Professor with the College of Electrical Engineering and Automation, Fuzhou University. His research interests include design, manufacturing, and control for power electronic system and components.

Dr. Mao was the recipient of one IEEE prize paper.